Moore and More (2024) 1:4
https://doi.org/10.1007/s44275-024-00007-y

ORIGINAL ARTICLE

Band engineering in two-dimensional porphyrin- and phthalocyanine-based covalent organic frameworks: insight from molecular design

Xiaojuan Ni[1] · **Jean-Luc Brédas**[1]

Received: 2 April 2024 / Revised: 17 May 2024 / Accepted: 22 May 2024

Abstract
Two-dimensional covalent organic frameworks (2D COFs) represent an emerging class of crystalline polymeric networks, characterized by their tunable architectures and porosity, synthetic adaptability, and interesting optical, magnetic, and electrical properties. The incorporation of porphyrin (Por) or phthalocyanine (Pc) core units into 2D COFs provides an ideal platform for exploring the relationship between the COF geometric structure and its electronic properties in the case of tetragonal symmetry. In this work, on the basis of tight-binding models and density functional theory calculations, we describe the generic types of electronic band structures that can arise in tetragonal COFs. Three tetragonal lattice symmetries are examined: the basic square lattice, the Lieb lattice, and the checkerboard lattice. The potential topological characteristics of each lattice are explored. The Por-/Pc-based COFs exhibit characteristic band dispersions that are directly linked to their lattice symmetries and the nature of the frontier molecular orbitals of their building units. We show that the band dispersions in these COFs can be tailored by choosing specific symmetries of the molecular building units and/or by modulating the relative energies of the core and linker units. These strategies can be extended to a wide array of COFs, offering an effective approach to engineering their electronic properties.

Keywords Covalent organic frameworks · Porphyrin · Phthalocyanine · Electronic band structures · Molecular design

1 Introduction

While porphyrin and phthalocyanine have electronic structures that are markedly different [1–5], they appear as structurally analogous macrocyclic compounds, each comprising four pyrrole-like subunits interconnected to form a 16-member inner ring [6–8]. These macrocycles exhibit pronounced absorption bands in the visible and have remarkable thermal and chemical stability [9, 10]. Importantly, their photophysical and redox properties can be finely tuned by selecting appropriate metal centers or peripheral substituents [11–15]. They have emerged as important components in molecular materials exhibiting compelling electronic and/or magnetic properties [16–18]. Incorporating porphyrin or phthalocyanine moieties into polymer networks significantly enhances the versatility of the resulting materials [19–24]. Covalent organic frameworks (COFs) based on these macrocycles, hereafter referred to as Por-COFs or Pc-COFs, provide for a broad range of applications from catalysis, adsorption, and separation processes to therapeutic uses [25–28]. The properties leading to specific applications can be optimized via preparation strategies, structural designs, and monomer functionalizations [9–11, 15, 29–34].

In addition to the applications stemming from their ultrahigh porosity, Por- or Pc-COFs with a tetragonal lattice symmetry are of significant interest in the framework of organic electronics and spintronics [35–42]. Two-dimensional (2D) COFs with Por or Pc four-arm cores typically display a square lattice symmetry, such as a Lieb lattice or checkerboard lattice, as illustrated in Fig. 1. A Lieb lattice has a unit cell that contains one corner site and two edge sites and can lead to various exotic electronic properties derived from its intriguing combination of Dirac and flat bands [43–45]. The first realization of a Lieb lattice

✉ Xiaojuan Ni
xjni@arizona.edu

✉ Jean-Luc Brédas
jlbredas@arizona.edu

[1] Department of Chemistry and Biochemistry, The University of Arizona, Tucson, AZ 85721-0041, USA

Published online: 04 July 2024

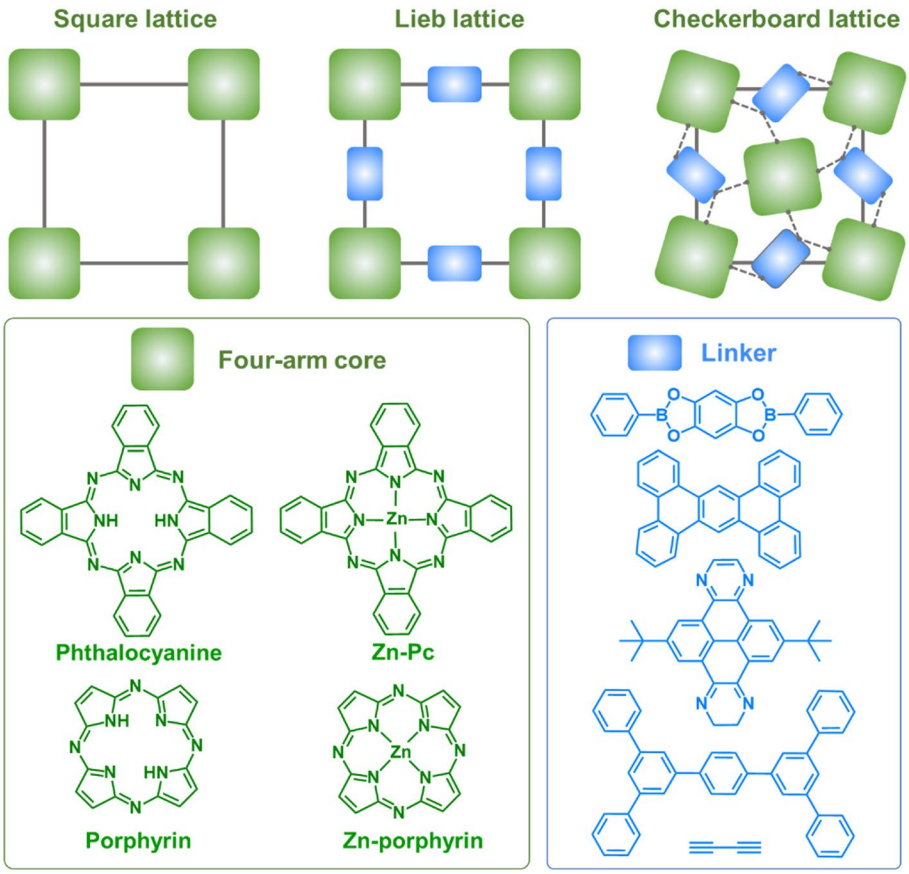

Fig. 1 Illustrations of typical lattice symmetries and representative cores and linkers for 2D tetragonal COFs. The four-arm cores and linkers are colored in green and blue, respectively. The grey square box in each lattice indicates the unit cell

in COFs was reported in 2017 by Jiang and co-workers in the case of a pyrene-based COF [35]; chemical oxidation of this semiconducting material with iodine significantly enhanced its electrical conductivity, with the radicals appearing on the pyrene cores resulting in a high spin density and paramagnetism [35]. Subsequent computational studies have shown that these Lieb-like COFs can undergo magnetic phase transitions as the carrier doping concentration increases [46, 47]. In a recent theoretical work, Heine and co-workers [48] reported that several Zn-Pc COFs can have characteristic Lieb-lattice electronic bands, which can be shifted to the Fermi level via electron removal or atom substitution. The checkerboard lattice (which corresponds to the line graph of the square lattice) [49] has been studied as a lattice model for antiferromagnetism or flat-band superfluidity [50, 51], although its material design and synthesis have remained limited [36, 52]. The first demonstration of a checkerboard lattice was reported in 2018 by Crommie and co-workers in the case of a single layer of COF-420 [36]; COF-420 consists of porphyrin-based core units that are bridged by chemically asymmetric linkers. A topographic image obtained from scanning tunneling spectroscopy revealed its distinct checkerboard pattern [36].

In the case of hexagonal COFs, based on the determination of the frontier molecular-orbital (MO) symmetry of the building blocks (core and linker units) and the lattice symmetry, we described recently how one can tailor the electronic bands (Dirac band *vs.* flat band) near the Fermi level by selecting appropriate molecular units [53]. Here, we expand this investigation to tetragonal COFs, with the aim of providing a comprehensive understanding of their electronic structures. First, the generic band structures related to the square lattice, Lieb lattice, and checkerboard lattice are examined using tight-binding (TB) models, since these models offer a theoretical framework for analyzing the electronic properties of the various lattices. Then, through an analysis of the frontier MOs of the building units of several representative Por- or Pc-COFs and with the assistance of the TB models, we qualitatively predict the band structures of the corresponding COFs. In the following step, density functional theory (DFT) calculations are employed to validate these TB predictions and demonstrate the realization of the anticipated generic band structures in the 2D polymer networks.

2 Computational approaches

The ground-state geometry optimizations and electronic-structure calculations of the porphyrin, Zn-porphyrin (Zn-Por), phthalocyanine, and Zn-phthalocyanine (Zn-Pc)

molecules were performed at the DFT level with the range-separated ωB97XD functional [54, 55] and the 6-31G** basis set (Gaussian16 package) [56]. The range-separation parameters (ω) were optimized nonempirically by minimizing $J(\omega) = \left[E_{HOMO}(\omega) + IP(\omega)\right]^2 + [E_{LUMO}(\omega) + EA(\omega)]^2$, where $E_{HOMO[LUMO]}$ is the energy of the highest occupied molecular orbital (HOMO) [lowest unoccupied MO (LUMO)] and IP [EA] is the vertical ionization potential [electron affinity] [57]. The ω values were optimized to be 0.180, 0.178, 0.127, and 0.125 bohr^{-1} for the Por, Zn-Por, Pc, and Zn-Pc, respectively. Considering the frontier MOs of the molecules, we employed tight-binding models to investigate their generic band structures in the various tetragonal lattices. Further details on the tight-binding models are provided in the Supplementary Information (SI).

Turning to the molecular building units (cores and linkers) of the Por-/Pc-COFs, their ground-state geometries and frontier MOs were also evaluated at the DFT level using the ωB97XD functional [54, 55] and the 6-31G** basis set [56]. The range-separation parameter (ω) for each building unit was set to the same value as that tuned for the corresponding Por, Zn-Por, Pc, or Zn-Pc molecule. DFT band structure calculations on the 2D Por-/Pc-COFs were then performed at the level of the generalized gradient approximation (GGA) with the Perdew–Burke–Ernzerhof (PBE) functional as implemented in the Vienna Ab initio Simulations Package (VASP) [58–60]. A Monkhorst-Pack k-points grid of $7\times7\times1$ and a plane-wave cutoff of 500 eV were used. To ensure full decoupling between neighboring slabs, a vacuum layer over 15 Å was adopted. All atoms were allowed to relax until the atomic forces for structural relaxation were reduced to less than 0.01 eV/Å. The VASPKIT code [61] was used for post-processing of the VASP-calculated data and the VESTA program [62], to visualize the results.

3 Results and discussion

3.1 Frontier molecular orbitals of the porphyrin and phthalocyanine molecules

The frontier MOs of the porphyrin and phthalocyanine molecules (which exhibit D_{2h} symmetry), are depicted in Fig. 2 along with those of their zinc-coordinated counterparts (D_{4h} symmetry). The figure also collects the MO energies and symmetries. It is worth noting that: (i) The Zn-coordinated molecules have a doubly degenerate lowest unoccupied MO (LUMO), which in the case of the lower-symmetry metal-free molecules splits into the energetically close LUMO and LUMO + 1 levels. In all four instances, the next unoccupied MO is energetically well separated. Similarly, the highest occupied molecular orbital (HOMO) and the HOMO-1 levels are well separated with an energy separation over 1.5 eV. (ii) In Zn-Por and Zn-Pc, zinc does not contribute to the wavefunctions of the frontier levels that are entirely determined by the π-conjugated macrocycle.

Building on the insight gained from previous studies [37, 41, 42, 53, 63, 64], these frontier MOs provide the orbital basis to initially elucidate the generic band dispersions in tetragonal Por- or Pc-COFs. In the next section, we illustrate various models where we consider one, two, or three orbitals per site. The relevance of these models to actual COFs will then be discussed later. We recall that, as was the case in our earlier work [63], the TB models look at the valence bands (VBs) and conduction bands (CBs) separately and can be different for the two cases.

3.2 Tight-binding model – square lattice

We begin with the simplest scenario, involving a single-orbital hopping (*e.g.*, the single HOMO depicted in Fig. 2) within a square lattice, see Fig. 3a. Thus, here, there is only one site per unit cell, each site carrying one orbital. As a result, this lattice model yields a single band, as shown in Fig. 3b. The eigenvalue for the simple square lattice model is $E\left(\vec{k}\right) = 2t(\cos k_1 + \cos k_2)$; $k_{1,2} = \vec{k}\cdot\overrightarrow{a_{1,2}}$, and $\overrightarrow{a_1} = \hat{x}$, $\overrightarrow{a_2} = \hat{y}$. The bandwidth corresponds to $8|t|$, *i.e.*, eight times the electronic coupling strength between sites; this feature is commonly observed in polymer networks with tetragonal symmetry [37, 42, 65]. We note that the band is flat along the Y-X k-path ($|k_1 \pm k_2| = \pi$), as illustrated in Fig. S1, which fulfills the phase cancellation condition (indeed, since $\cos k_2 = -\cos k_1$, this leads to $E\left(\vec{k}\right) = 0$) [66].

For the next model, we consider the case where two frontier π_x and π_y molecular orbitals (MOs) need to be considered as the orbital basis (see Fig. 3c); these can be, for example, the degenerate LUMOs of Zn-Por or Zn-Pc. Here, two bands emerge with eigenvalues $E_{1[2]} = 2 * (pp\sigma * \cos k_{1[2]} + pp\pi * \cos k_{2[1]})$. Under the condition $|k_1| = |k_2|$ along Γ-$M_{1[2]}$, the two bands are degenerate along the Γ-M k-path, as depicted in Fig. 3d. In the case of a negligible $pp\pi$ hopping integral, the bandwidth corresponds to $4|\ pp\sigma|$. We note that, when the core unit possesses only two-fold symmetry such as in Por or Pc and we need to consider the energetically close LUMO and LUMO + 1, since the degeneracy of these π orbitals is lifted, there appears an energetic splitting of the two bands along the Γ-M k-path (see Fig. S2c).

By incorporating an additional σ orbital, we can extend the orbital basis to (σ, π_x, π_y), as illustrated in Fig. 3e. This can be viewed as a combination of the earlier two lattice models with a single orbital and degenerate π orbitals and would have to be used, for instance, if a doubly degenerate LUMO is energetically close to the LUMO + 1. Then, the relative on-site energies of the σ and π orbitals, together with

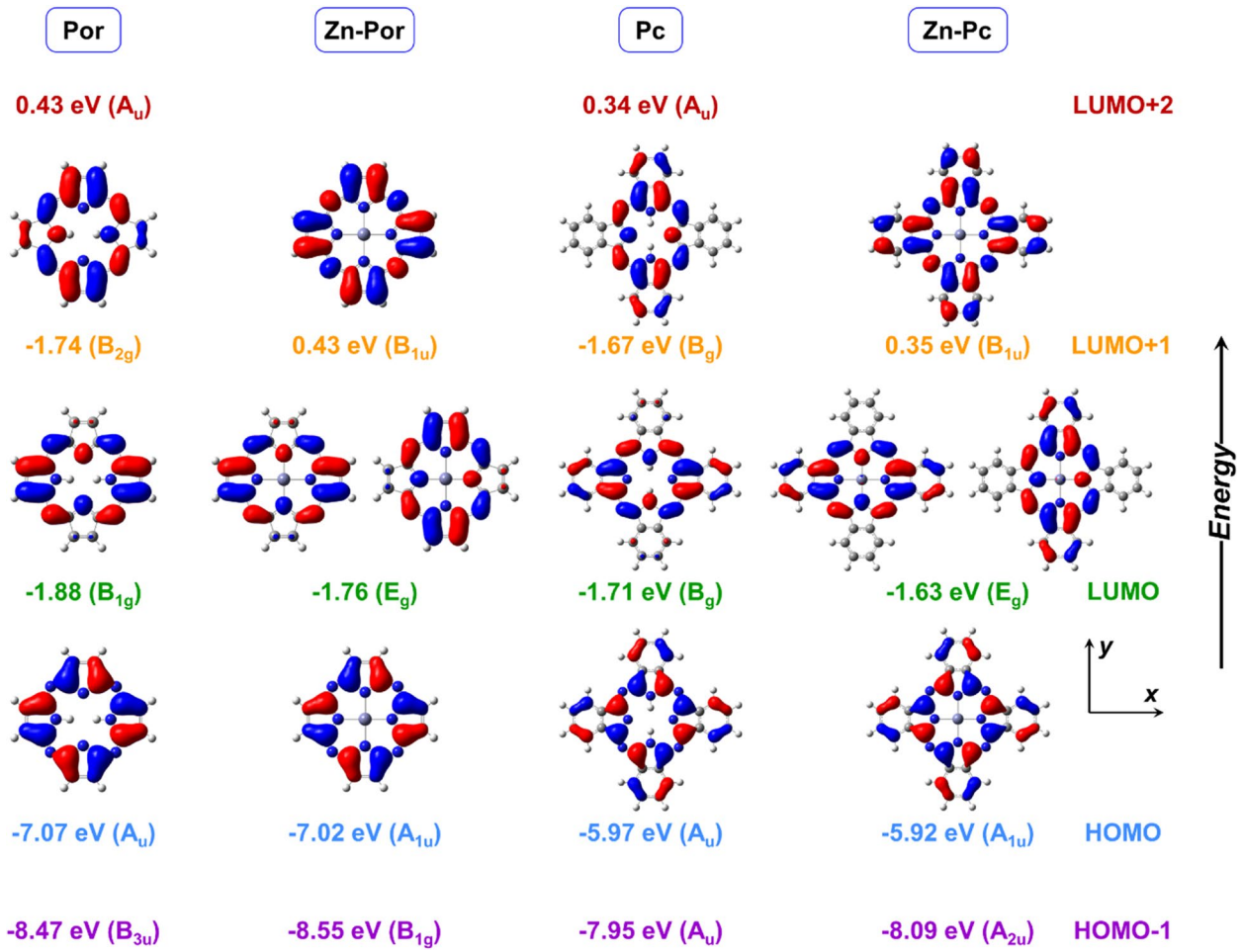

Fig. 2 Frontier molecular orbitals of the Por, Zn-Por, Pc, and Zn-Pc molecules, as calculated at the ωB97XD level of theory with the 6-31G** basis set. The MO energies and symmetries are also given. The black arrows indicate our convention for the x and y axes. (The wavefunctions of the HOMO-1 and LUMO + 2 levels are omitted as these levels are not considered in any of the subsequent calculations)

the differences in hopping integrals, can result in a variety of band dispersions, such as the one shown in Fig. 3f.

Given that the HOMO and LUMO levels of the Por and Pc systems exhibit opposite orbital parities (where orbital parity refers to the evolution of the wavefunction under spatial inversion, with even parity keeping the wavefunction the same upon inversion and odd parity changing the sign of the wavefunction), they provide the essential foundation for the emergence of topological states due to band inversion (see Fig. S3) [39, 41]. The (σ, π_x, π_y)-orbital basis in COFs is analogous to the (s, p_x, p_y)-orbital basis in inorganic materials, such as the Au/GaAs(111) interfacial system (even though the latter corresponds to a trigonal lattice) [67]. In Au/GaAs(111), the s- and p-orbital components of the three bands near the Fermi level were described effectively via an sp^2 hybridization involving Au-s and As-p orbitals. Given the substantial spin-orbit coupling (SOC) effect in both Au and GaAs, the degeneracy at the Dirac point in the band structure is lifted, resulting in the formation of a topological insulating gap. Details regarding topological features in a square lattice with a (σ, π_x, π_y)-orbital basis are provided in the SI.

3.3 Tight-binding model – Lieb lattice

The Lieb lattice is a variant of the square lattice that consists of three sites within each square unit cell, as illustrated in Fig. 4a. Two of the sites (highlighted in blue) are connected to two neighboring sites, while the third site (marked in green) has four neighbors. Hereafter, these sites will be referred to as edge (blue) and corner (green) sites, respectively. When considering hopping only between nearest-neighbor (NN) sites, this geometric arrangement gives rise to an electronic band structure characterized by two distinctive features: (i) two dispersive bands forming a Dirac cone at the M point in the first Brillouin zone and (ii) a flat band intersecting the Dirac point (Fig. 4b). The flat band

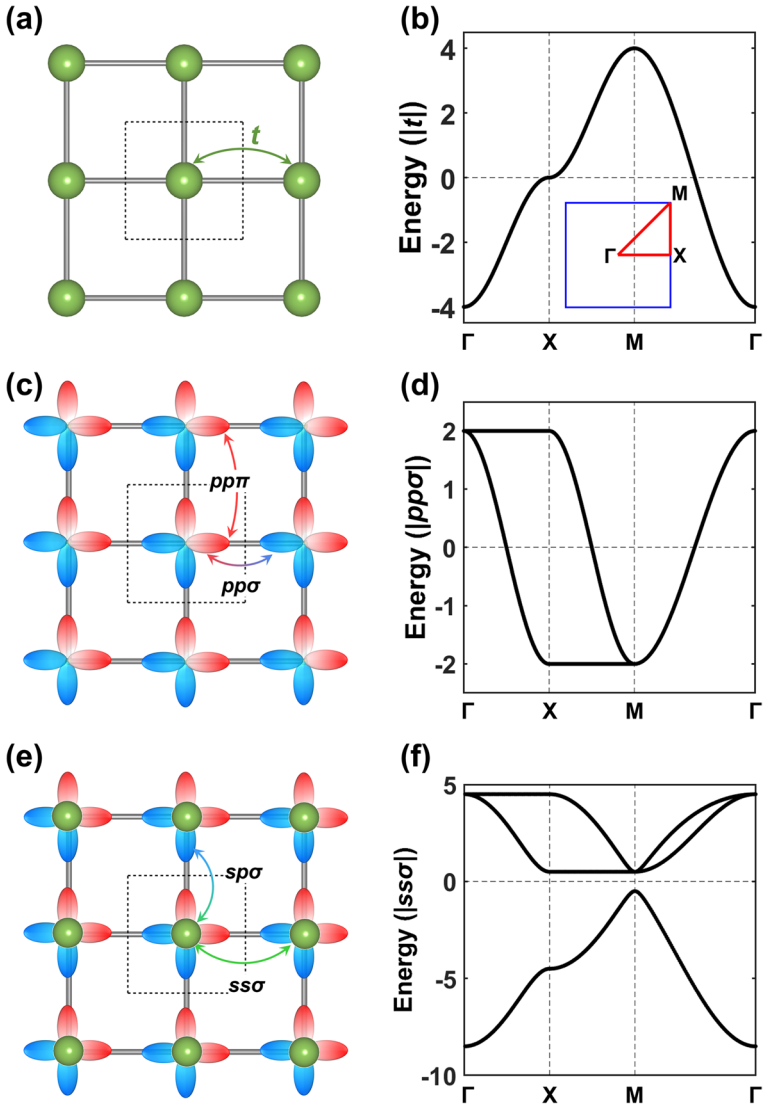

Fig. 3 Illustrations of (**a**) single-orbital hopping, (**c**) (π_x, π_y)-orbital hopping, and (**e**) (σ, π_x, π_y)-orbital hopping in a square lattice. The hopping integrals are indicated by arrows. The dashed square indicates the unit cell. The corresponding band structures obtained from TB models with (**b**) $\varepsilon_0 = 0$ and $t > 0$; (**d**) $\varepsilon_\pi = 0$, $pp\sigma > 0$, and $pp\pi = 0$; and (**f**) $\varepsilon_\sigma = -4.5|ss\sigma|$, $\varepsilon_\pi = 2.5|ss\sigma|$, $ss\sigma < 0$, $sp\sigma = |ss\sigma|$, $pp\sigma = |ss\sigma|$, and $pp\pi = 0$. The inset in (**b**) depicts the first Brillouin zone. The $pp\sigma$, $pp\pi$, $ss\sigma$ and $sp\sigma$ hopping integrals are indicated by the arrows in (**c**) and (**e**)

comprises electronic states localized exclusively on edge sites, whereas all sites contribute to the dispersive bands.

A SOC term can be incorporated into the Hamiltonian by considering an imaginary hopping between the second nearest-neighbor (2NN) sites (see Fig. 4a), in the spirit of the SOC term found in the Kane-Mele model [68]. The SOC effects can generally lift the degeneracy at the Dirac point, as illustrated in Fig. 4c and result in the opening of what are topologically non-trivial bandgaps above and below the flat band.

We recall that a topologically non-trivial bandgap is characterized by a topological invariant. In systems with inversion symmetry, the topological invariant known as the Z_2 number [69] can be determined based on the parity at time-reversal invariant momenta [70]. A system with a nontrivial topology ($Z_2 = 1$) represents a topological insulating phase that exhibits the quantum spin Hall effect. This phase is characterized by edge states with quantized conductivity. Additionally, the Z_2 number is equivalent to the spin Chern number, $C_s = \frac{1}{2}(C_\uparrow - C_\downarrow)$. The Chern number is defined as: [71] $C = \frac{1}{2\pi}\int_{BZ} d^2k F_{12}(k)$, where $F_{12}(k) = \frac{\partial}{\partial k_1}A_2(k) - \frac{\partial}{\partial k_2}A_1(k)$ is the Berry curvature; $A_\mu(k) = -i\langle n_k|\frac{\partial}{\partial k_\mu}|n_k\rangle$, the Berry connection; and $|n_k\rangle$, the normalized wave function of the respective band.

We also examined scenarios with different on-site energies for edge and corner sites, which reflects the differences present between the COF core and linker units. In this context, the degeneracy of the Dirac and flat bands is disrupted, leading to a trivial bandgap characterized by a zero topological invariant, as depicted in Fig. 4d and e. The position of the bandgap, either below ($\varepsilon_{corner} < \varepsilon_{edge}$) or above ($\varepsilon_{corner} > \varepsilon_{edge}$) the flat band, is determined by the relative on-site energies between the two types of sites. Near the M point, the wavefunction components of these Dirac and flat bands are found to be markedly distinct from those of the ideal Lieb lattice model (see Fig. 4b). Specifically, the

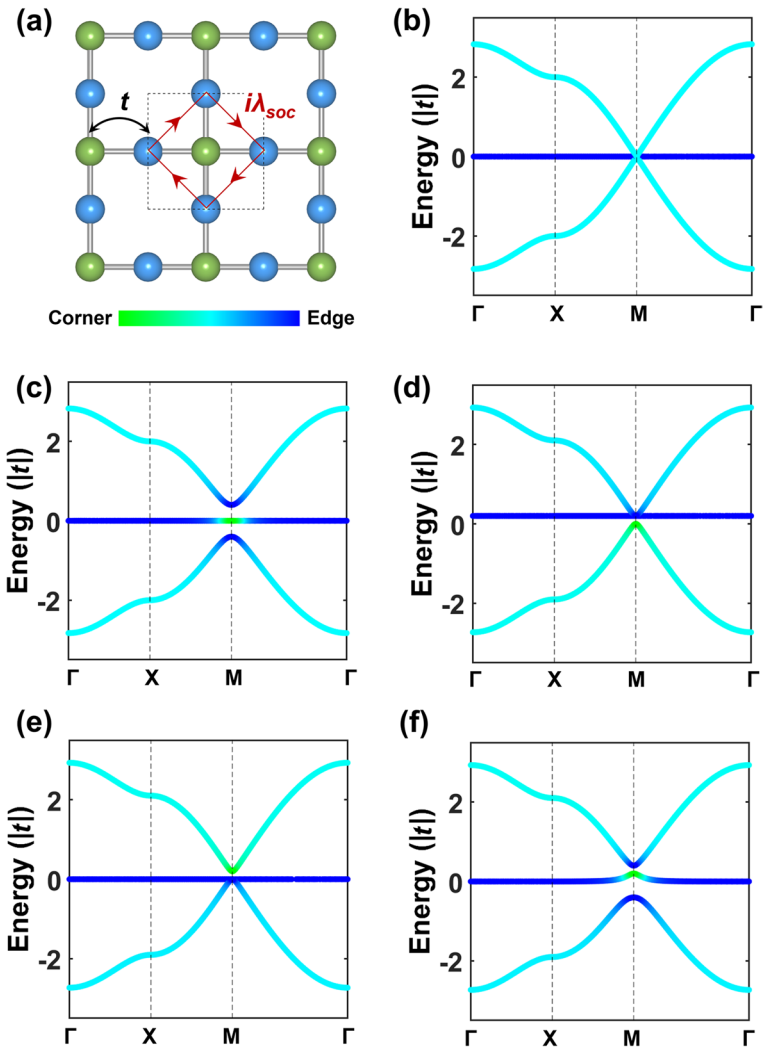

Fig. 4 **a** Illustration of a single-orbital hopping in the Lieb lattice. The hopping integral is indicated by the black arrow. The spin-orbit coupling (SOC) term is considered as an imaginary hopping between the second nearest-neighbor sites, indicated by red arrows; λ_{SOC} represents the magnitude of the SOC. The corner and edge sites are colored in green and blue, respectively. Examples of band structures obtained from the Lieb lattice models: (**b**) $\varepsilon_{corner/edge} = 0$ and $\lambda_{SOC} = 0$; (**c**) $\varepsilon_{\text{corner/edge}} = 0$ and $\lambda_{SOC} = 0.1|t|$; (**d**) $\varepsilon_{corner} = 0$, $\varepsilon_{edge} = 0.2|t|$, and $\lambda_{SOC} = 0$; (**e**) $\varepsilon_{corner} = 0.2|t|$, $\varepsilon_{edge} = 0$, and $\lambda_{SOC} = 0$; and (**f**) $\varepsilon_{corner} = 0.2|t|$, $\varepsilon_{edge} = 0$, and $\lambda_{SOC} = 0.1|t|$

wavefunction at the M point of the separated Dirac band (the bottommost band in Fig. 4d or the topmost band in Fig. 4e) primarily comes from the corner sites, while the edge sites predominantly contribute to the flat band and the other Dirac band.

We also considered a case where a SOC term is incorporated in addition to the on-site energy difference. The resulting band structure has three isolated bands, as depicted in Fig. 4f; the two bandgaps at the M point correspond to a topological insulating phase with a nonzero Z_2 number. By adjusting the parameters of the on-site energy difference and the SOC strength, the Chern number of the middle flat band can be either zero or nonzero [46].

Given the four-fold symmetry of the corner site in a Lieb lattice, the doubly degenerate frontier MOs of the four-arm core units can also emerge in tetragonal COFs. We examined a special case of the Lieb lattice where the corner site carries degenerate (π_x, π_y)-orbitals and the edge site contains a single orbital, as depicted in Fig. 5a. By considering only the NN interactions between corner and edge sites, while excluding interactions between corner-to-corner or edge-to-edge sites, the band structure obtained from the TB model is presented in Fig. 5b. This band structure is markedly different from those shown in Fig. 4. Therefore, the relative on-site energies for the corner and edge sites as well as the MO degeneracy of the corner site play an important role in determining the electronic band structure of the Lieb lattice.

3.4 Tight-binding model – checkerboard lattice

A checkerboard lattice is created by introducing additional sites at the center of each square in the basic square lattice, as depicted in Fig. 6a. When considering only NN hopping, the TB model in the case of a single orbital per site yields the two bands shown in Fig. 6b; the bands have a folded structure derived from those shown in Fig. 3b. If the 2NN hopping parameter is non-zero, the partial flat band at half filling gains some dispersion, as illustrated in Fig. S4a. By extending the orbital basis to include two (π_x, π_y) or three (σ, π_x, π_y) orbitals per site, the typical band structures that

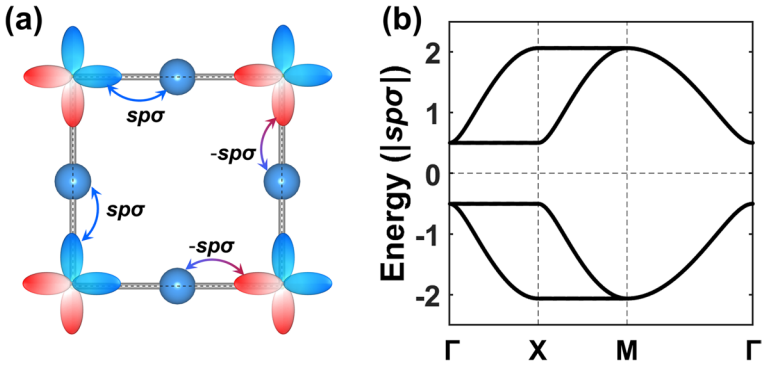

Fig. 5 **a** Illustration of (σ, π_x, π_y)-orbital hopping in the Lieb lattice. The corner site carries degenerate (π_x, π_y)-orbitals and the edge site, a single orbital. Only nearest-neighbor interactions are considered; the hopping integral $sp\sigma$ is indicated by the arrows between the corner and edge sites. **b** Band structures obtained from this lattice model: $\varepsilon_\sigma = 0.5|sp\sigma|$, $\varepsilon_\pi = -0.5|sp\sigma|$, and $sp\sigma > 0$

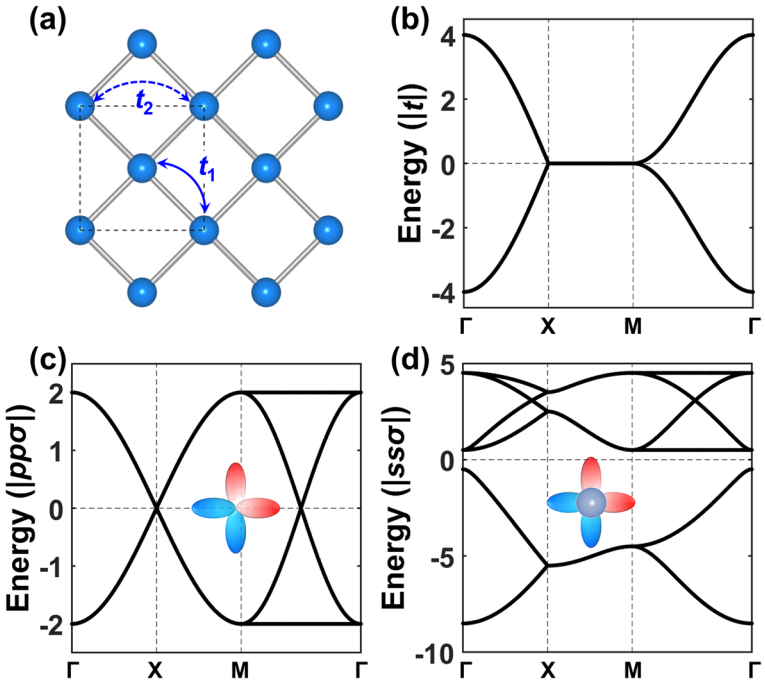

Fig. 6 **a** Illustration of the single-orbital hopping model in the checkerboard lattice; the nearest-neighbor hopping integral is indicated by t_1 and the second nearest-neighbor hopping, by t_2. Band structures obtained from the checkerboard lattice models: (**b**) single-orbital hopping with nearest-neighbor hopping integral $t_1 > 0$ and $\varepsilon_0 = 0$; (**c**) (π_x, π_y)-orbital hopping with $\varepsilon_\pi = 0$, $pp\sigma > 0$, and $pp\pi = 0$; (**d**) (σ, π_x, π_y)-orbital hopping with $\varepsilon_\sigma = -4.5|ss\sigma|$, $\varepsilon_\pi = 2.5|ss\sigma|$, $ss\sigma < 0$, $sp\sigma = |ss\sigma|$, $pp\sigma = |ss\sigma|$, and $pp\pi = 0$

can be obtained are depicted in Fig. 6c and d, respectively. Similarly, the partial flat bands along the M-Γ k-path gain some dispersion when considering a nonzero $pp\pi$ parameter (see Fig. S4b).

It is worth noting that the band structure derived from the checkerboard lattice model exhibits similarities with those of materials possessing a Cairo pentagonal lattice symmetry. In each 2D pentagonal lattice (see Fig. S5), there are two types of sites: one is fourfold-coordinated and the other is threefold-coordinated, with a total of six sites per unit cell. The fourfold-coordinated sites display the checkerboard lattice symmetry. Considering one orbital per site, this lattice model yields six bands. For reference, the checkerboard lattice with a (σ, π_x, π_y)-orbital basis also produces six bands, which indeed look like those obtained from the pentagonal lattice model [40]. Since the theoretical prediction of penta-graphene in 2015 by Zhang and co-workers [72], a variety of other 2D pentagonal materials have been theoretically predicted and/or experimentally synthesized [73–77]. These materials are reported to exhibit tunable properties ranging from semiconducting to metallic and even topologically insulating states [78].

3.5 Covalent organic frameworks

We selected three COFs with either Zn-Por or Zn-Pc as the four-arm core units to serve as representative examples. These examples were chosen to demonstrate that the characteristic band dispersions associated with the square lattice, the Lieb lattice, and the checkerboard lattice, which we described above, can be realized in 2D polymer networks.

3.5.1 Square lattice

The first COF we examined is built from zinc-5,10,15,20-tetraethynylporphyrin (Zn-TEP) units (we refer to it as Zn-TEP COF) [38]. Its chemical structure is illustrated in Fig. 7a. Prior to conducting band-structure calculations, we first evaluated the frontier MOs of the Zn-TEP unit, as shown in Fig. S6. Based on the understanding gained from the TB models we discussed above, we can predict the characteristics of the bands appearing near the Fermi level. Following the square lattice model with single-orbital hopping (see Fig. 3b), the topmost VB of the Zn-TEP COF is anticipated to be a single band derived from the Zn-TEP HOMO. The two lowest CBs are expected to originate from the degenerate LUMO levels of Zn-TEP, following the (π_x, π_y)-orbital hopping model in a square lattice, which results in the typical band dispersions illustrated in Fig. 3d.

The DFT-calculated band structure of Zn-TEP is presented in Fig. 7b and confirms our predictions: The lowest two CBs display the characteristic band dispersion arising from a square lattice model with degenerate (π_x, π_y)-orbital hopping, while the top VB is solely derived from the HOMO of the Zn-TEP. Figure 7c displays the wavefunctions of bands 1 to 4 at the Γ point. We note that band 3 is a flat band, originating from the HOMO-1 level of Zn-TEP; this flatness is related to the fact that the acetylene units do not contribute to the HOMO-1 wavefunction (see Fig. S6) [42]. A comparison of the Γ-point wavefunctions with the frontier MOs of Zn-TEP (Fig. 7c vs. Fig. S6) corroborates that the electronic bands near the Fermi level are indeed derived from the frontier MOs of the corresponding building unit. This confirms that, by examining the characteristics of the frontier MOs of the building units along with the COF lattice symmetry, one can effectively predict the band characteristics in the corresponding COF with the assistance of TB models.

3.5.2 Lieb lattice

We recall that the Lieb lattice has two types of sites: corner sites and edge sites. For the interaction between these sites to be effective, it is essential to have a close alignment of their on-site energies; this facilitates the desired electronic coupling between the two types of sites and leads to the emergence of electronic bands characteristic of the Lieb lattice. Therefore, to realize the electronic features of a Lieb lattice in a 2D COF, it is important to select a linker unit with an on-site energy comparable to that of the core unit. The Zn-Pc-based COF with pyrazine-pyrene-pyrazine linkers [79] illustrated in Fig. 8a, is a pertinent example in this regard. The frontier MOs of the building units are shown in Fig. S7. Given that the Zn-Pc HOMO level is much higher in energy than that of the pyrene-pyrazine linker (by over 1 eV), the top VB is expected to be exclusively derived from the former level. Subsequently, the appropriate model for the top VB in fact corresponds to a single orbital hopping in a square lattice, with the anticipation that the band will be flat as only the corner sites will contribute to it. Turning to the unoccupied levels, the degenerate Zn-Pc LUMOs levels are lower in energy than the linker LUMO but with a smaller energetic separation of approximately 0.7 eV; thus, the bottom CBs of this COF can be expected to display a band structure akin to that illustrated in Fig. 5b. In addition, since the LUMO + 1 level of Zn-Pc and the LUMO + 2 level of the linker are rather closely aligned (with a separation of about 0.48 eV), the electronic states derived from these orbitals are anticipated to exhibit Lieb-like characteristics.

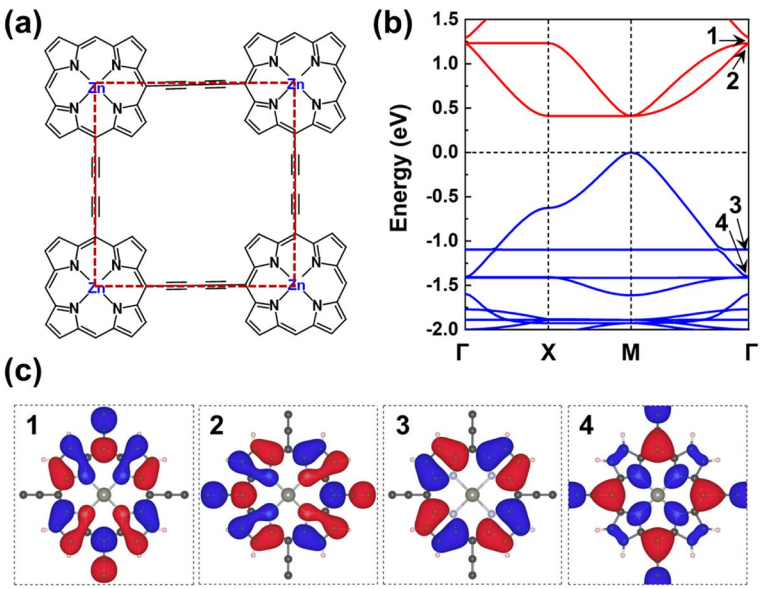

Fig. 7 Two-dimensional Zn-TEP COF: **a** Chemical structure; the red dashed box represents the unit cell. **b** DFT-PBE-calculated band structure; the VBs and CBs are colored in blue and red, respectively. **c** Illustration of the wavefunctions at the Γ point for bands **1** to **4**, as labelled in (**b**)

The DFT-calculated band structure is shown in Fig. 8b. Indeed, the dispersions of the upper unoccupied bands in the energy window between 2 and 3.5 eV for the CBs exhibit three bands (denoted 1 to 3) possessing the characteristics of a Lieb lattice. An analysis of their wavefunctions at the Γ point, shown in Fig. 8c, reveals that bands 1 and 3 originate from both the core and linker units, while band 2 is predominantly contributed by the LUMO + 2 level of the linker units; these attributes are consistent with those depicted in Fig. 4e.

The wavefunctions of the bands near the Fermi level are depicted in Fig. S8. As predicted, the topmost VB consists of a single band originating solely from the Zn-Pc HOMO. The bottom CBs can be classified into three groups (CB, CB + 1, and CB + 2), each containing two bands. There exists a close correspondence between these CBs and the Zn-Pc LUMO and the LUMO and LUMO + 1 levels of the pyrazine-pyrene-pyrazine linker (see Fig. S7). In contrast to the width of approximately 1 eV seen for the Lieb bands, the widths of the CBs and VBs near the Fermi level are much narrower and smaller than 0.1 eV. This can be attributed to the very limited electronic coupling between the pyrazine-pyrene-pyrazine-based linkers and Zn-Pc units. By modulating the degree of conjugation in the linker unit (*i.e.*, by varying the linker length), the relative positions of the three bands derived from the Lieb lattice can be adjusted to be in closer proximity to the Fermi level [48]. Again, in the framework of the COF lattice symmetry, the analysis of the symmetries and energies of the frontier MOs of the core and linker units allows for the prediction of the band dispersion near the Fermi level in a specific COF.

3.5.3 Checkerboard lattice

When the core units situated at both the center and corner sites are identical, the primitive unit cell of the COF adopts the structure of a simple square lattice. However, introducing a relative orientation between these two sites, as exemplified by the Zn-Pc-based anthracene-linked COF [40] depicted in Fig. 9a, leads to a unit cell with the symmetry of a checkerboard lattice. The frontier MOs of the Zn-Pc core and the tribenzo[f,k,m]tetraphene linker are shown in Fig. S9. The degenerate Zn-Pc LUMO levels are significantly lower in energy than the linker LUMO (difference of *ca.* 1.6 eV), while the Zn-Pc HOMO is higher than that of the linker by about 1 eV. Thus, the bottom CBs and top VBs of this ZnPc-based anthracene-linked COF are expected to display band dispersions similar to those depicted in Fig. 6.

The band structure calculated at the DFT-PBE level of theory is shown in Fig. 9b and indeed exhibits features like those in Fig. 6. Figure 9c presents the wavefunctions corresponding to bands 1 to 6 at the Γ point and confirms that the bottom CBs originate from the degenerate LUMOs of Zn-Pc, while the top VBs are derived from the single HOMO of Zn-Pc. The wavefunctions at the Γ point for bands 7 and 8, depicted in Fig. S10, clearly carry the orbital characteristics of the HOMO level of the tribenzo[f,k,m]tetraphene linker. These results underline again that the most relevant characteristics of the band structure of a specific COF can be qualitatively predicted by analyzing the symmetry and

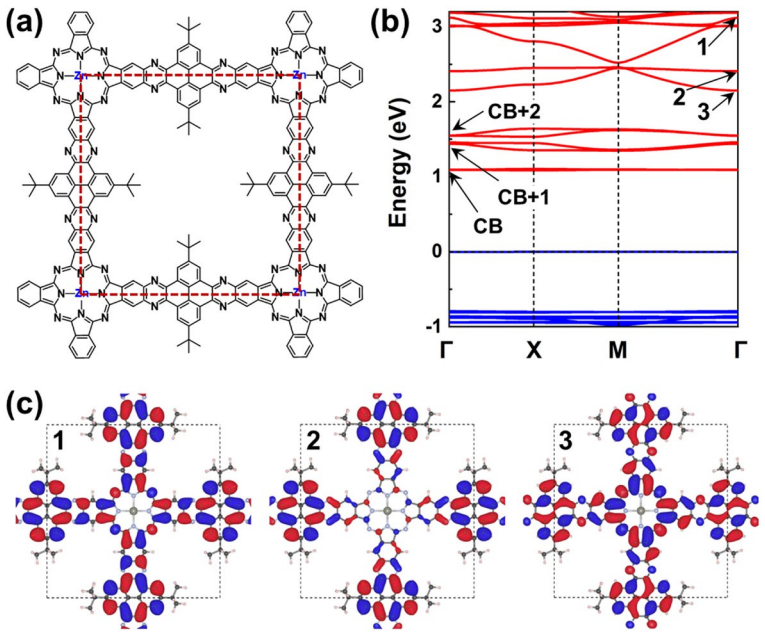

Fig. 8 Two-dimensional Zn-Pc-based pyrazine-linked COF: **a** Chemical structure; the red dashed box represents the unit cell. **b** DFT-PBE-calculated band structure; the VBs and CBs are colored in blue and red, respectively. **c** Illustration of the wavefunctions at the Γ point for bands **1** to **3**, as labelled in (**b**)

energy of the frontier MOs of its building units in conjunction with the lattice symmetry.

In the case of Por-/Pc-based COFs with two-fold symmetric porphyrin or phthalocyanine as four-arm core units, the band structures closely resemble those of COFs with Zn-Por/Pc as core units [41, 80], despite the lifted degeneracy at the M point due to the energy splitting between the LUMO and LUMO + 1 levels in the metal-free porphyrin and phthalocyanine molecules (Fig. 2). The comparison between Zn-Pc-based and Pc-based COFs is presented in Figs. S11 and S12.

While our present work focuses on the electronic structure of COF monolayers, we have also briefly investigated the impact of the interlayer stacking patterns on the electronic properties by using Zn-TEP COF as a representative example, as detailed in the SI. Due to the relatively small bandgap of these Pc-based COFs, they are promising materials to achieve band inversion and a topological state. A topological phase transition from a conventional insulating state to a topological Dirac semimetal state has been theoretically predicted to occur in a Pc-based COF upon the application of external strain [41]. However, it is worth bearing in mind that the realization of a first-order topological insulating phase usually requires a significant SOC strength to facilitate the band inversion and bandgap opening. In this regard, it is thus challenging to achieve a topological insulating state in COFs composed solely of light elements (such as H, C, N, O, and F) or where only light elements contribute to the frontier wavefunctions. We note that incorporating heavy metal atoms with a strong SOC effect is an effective approach to realizing a topological insulating phase in porphyrin/phthalocyanine-based metal-organic frameworks (MOFs). For instance, phthalocyanine-based MOFs with metal centers other than zinc have been studied and shown to exhibit a topological insulating phase, leading to the quantum spin/anomalous Hall effect [39, 81].

4 Conclusions

Employing tight-binding models and density functional theory calculations, we have investigated the electronic structures of tetragonal COFs, using porphyrin- and phthalocyanine-based COFs as representative examples. The

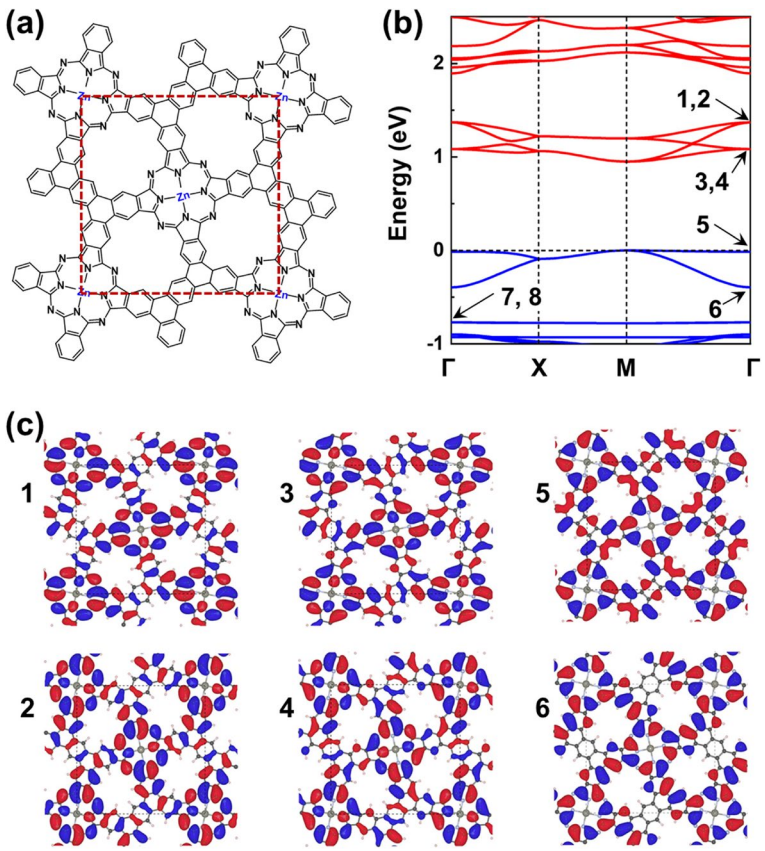

Fig. 9 Two-dimensional ZnPc-based anthracene-linked COF: **a** Chemical structure; the red dashed box represents the unit cell. **b** DFT-PBE-calculated band structure; the VBs and CBs are colored in blue and red, respectively. **c** Illustration of the wavefunctions at the Γ point for bands **1** to **6**, as labelled in (**b**)

generic band structures corresponding to the square lattice, the Lieb lattice, and the checkerboard lattice were initially explored through tight-binding model analyses. The realization of these band structures was demonstrated in 2D polymer networks that incorporate porphyrin or phthalocyanine as building units, thereby confirming the versatility and applicability of these TB models in the context of COFs.

Expanding on our earlier investigations of hexagonal COFs, we have determined that the band structures in tetragonal COFs can also be tailored by choosing the symmetries of the core units and/or by adjusting the relative energies of the frontier MOs of the core and linker units. The approaches taken to engineer the band structures outlined in this and our previous studies are expected to be applicable to a wide variety of COFs, thereby broadening the ability to tune the electronic properties and enhancing the functionality of these materials.

Finally, we emphasize that, unlike the first-order topological insulating phase that requires a substantial spin-orbit coupling effect to achieve band inversion and bandgap opening, the topological semimetal phase and higher-order topological insulating phase can be realized in COFs composed exclusively of light elements [41, 63, 82].This distinction highlights the versatility of COFs in accommodating various topological phases, thereby expanding their potential applications in the realm of topological materials science.

Supplementary Information The online version contains supplementary material available at https://doi.org/10.1007/s44275-024-00007-y.

Acknowledgements We gratefully acknowledge the Research Data Center at The University of Arizona for providing high-performance computing resources.

Authors' contributions Xiaojuan Ni: Conceptualization, Investigation, Formal analysis, Visualization, and Writing- Original draft preparation, Reviewing, and Editing.

Jean-Luc Brédas: Conceptualization, Supervision, Writing- Reviewing and Editing.

Funding This work was supported by the College of Science at the University of Arizona.

Availability of data and materials The data supporting the findings of this article are available within the article and its supplementary materials.

Declarations

Ethics approval and consent to participate Ethics statement for the use of human and animal subjects (may require consent to participate and consent to publish for human subjects). This declaration is "not applicable".

Competing interests The authors have no competing interests to declare that are relevant to the content of this article.

References

1. Gouterman M (1959) Study of the effects of substitution on the absorption spectra of porphin. J Chem Phys 30:1139–1161. https://doi.org/10.1063/1.1730148
2. Gouterman M (1961) Spectra of Porphyrins. J Mol Spectrosc 6:138–163. https://doi.org/10.1016/0022-2852(61)90236-3
3. Gouterman M, Wagnière GH, Snyder LC (1963) Spectra of porphyrins: part II. Four orbital model. J Mol Spectrosc 11:108–127. https://doi.org/10.1016/0022-2852(63)90011-0
4. Weiss C, Kobayashi H, Gouterman M (1965) Spectra of porphyrins: part III. Self-consistent molecular orbital calculations of porphyrin and related ring systems. J Mol Spectrosc 16:415–450. https://doi.org/10.1016/0022-2852(65)90132-3
5. Ortí E, Brédas JL (1988) Electronic structure of metal-free phthalocyanine: a valence effective hamiltonian theoretical study. J Chem Phys 89:1009–1016. https://doi.org/10.1063/1.455251
6. Thomas AL (1990) Phthalocyanine research and applications. CRC Press, United States
7. McKeown NB (1998) Phthalocyanine materials: synthesis, structure and function. Cambridge University Press, Cambridge
8. Kadish K, Smith KM, Guilard R (2003) The porphyrin Handbook. Elsevier Inc, Amsterdam
9. Darwent JR, Douglas P, Harriman A, Porter G, Richoux M-C (1982) Metal phthalocyanines and porphyrins as photosensitizers for reduction of water to hydrogen. Coord Chem Rev 44:83–126. https://doi.org/10.1016/S0010-8545(00)80518-4
10. Bonnett R (1995) Photosensitizers of the porphyrin and phthalocyanine series for photodynamic therapy. Chem Soc Rev 24:19–33. https://doi.org/10.1039/CS9952400019
11. Gassman PG, Ghosh A, Almlof J (1992) Electronic effects of peripheral substituents in porphyrins: x-ray photoelectron spectroscopy and Ab Initio self-consistent field calculations. J Am Chem Soc 114:9990–10000. https://doi.org/10.1021/ja00051a035
12. Cho HS, Jeong DH, Cho S, Kim D, Matsuzaki Y, Tanaka K, Tsuda A, Osuka A (2002) Photophysical properties of porphyrin tapes. J Am Chem Soc 124:14642–14654. https://doi.org/10.1021/ja020826w
13. Liao M-S, Scheiner S (2002) Electronic structure and bonding in metal porphyrins, Metal=Fe Co, Ni, Cu, Zn. J Chem Phys 117:205–219. https://doi.org/10.1063/1.1480872

14. Li J, Zhang S-L (2010) Conductivity exponents in stick percolation. Phys Rev E Stat Nonlin Soft Matter Phys 81(2 Pt 1):021120. https://doi.org/10.1103/PhysRevE.81.021120
15 Kar P, Sardar S, Alarousu E, Sun J, Seddigi ZS, Ahmed SA, Danish EY, Mohammed OF, Pal SK (2014) Impact of metal ions in porphyrin-based applied materials for visible-light photocatalysis: key information from ultrafast electronic spectroscopy. Chemistry 20:10475–10483. https://doi.org/10.1002/chem.201402632
16. Yella A, Lee H-W, Tsao HN, Yi C, Chandiran AK, Nazeeruddin MdK, Diau EW-G, Yeh C-Y, Zakeeruddin SM, Grätzel M (1979) Porphyrin-sensitized solar cells with cobalt (II/III)–based redox electrolyte exceed 12 percent efficiency. Science 2011(334):629–634. https://doi.org/10.1126/science.1209688
17. Li L-L, Diau EW-G (2013) Porphyrin-sensitized solar cells. Chem Soc Rev 42:291–304. https://doi.org/10.1039/C2CS35257E
18. Sorokin AB (2013) Phthalocyanine metal complexes in catalysis. Chem Rev 113:8152–8191. https://doi.org/10.1021/cr4000072
19. Grill L, Dyer M, Lafferentz L, Persson M, Peters MV, Hecht S (2007) Nano-architectures by covalent assembly of molecular building blocks. Nat Nanotechnol 2:687–691. https://doi.org/10.1038/nnano.2007.346
20. Perepichka DF, Rosei F (1979) Extending polymer conjugation into the second dimension. Science 2009(323):216–217. https://doi.org/10.1126/science.1165429
21. Spitler EL, Dichtel WR (2010) Lewis acid-catalysed formation of two-dimensional phthalocyanine covalent organic frameworks. Nat Chem 2:672–677. https://doi.org/10.1038/nchem.695
22 Spitler EL, Colson JW, Uribe-Romo FJ, Woll AR, Giovino MR, Saldivar A, Dichtel WR (2012) Lattice expansion of highly oriented 2D phthalocyanine covalent organic framework films. Angew Chem Int Ed 51:2623–2627. https://doi.org/10.1002/anie.201107070
23. So MC, Jin S, Son H-J, Wiederrecht GP, Farha OK, Hupp JT (2013) Layer-by-layer fabrication of oriented porous thin films based on porphyrin-containing metal-organic frameworks. J Am Chem Soc 135:15698–15701. https://doi.org/10.1021/ja4078705
24. Chen R, Shi J-L, Ma Y, Lin G, Lang X, Wang C (2019) Designed synthesis of a 2D porphyrin-based Sp2 carbon-conjugated covalent organic framework for heterogeneous photocatalysis. Angew Chem Int Ed 58:6430–6434. https://doi.org/10.1002/anie.201902543
25. Li B-Q, Zhang S-Y, Wang B, Xia Z-J, Tang C, Zhang Q (2018) A porphyrin covalent organic framework cathode for flexible Zn–air batteries. Energy Environ Sci 11:1723–1729. https://doi.org/10.1039/C8EE00977E
26. Jia H, Yao Y, Zhao J, Gao Y, Luo Z, Du P (2018) A novel two-dimensional nickel phthalocyanine-based metal-organic framework for highly efficient water oxidation catalysis. J Mater Chem A Mater 6:1188–1195. https://doi.org/10.1039/c7ta07978h
27. Zhong H, Ly KH, Wang M, Krupskaya Y, Han X, Zhang J, Zhang J, Kataev V, Büchner B, Weidinger IM, Kaskel S, Liu P, Chen M, Dong R, Feng X (2019) A phthalocyanine-based layered two-dimensional conjugated metal-organic framework as a highly efficient electrocatalyst for the oxygen reduction reaction. Angew Chem Int Ed 58:10677–10682. https://doi.org/10.1002/anie.201907002
28. Han B, Ding X, Yu B, Wu H, Zhou W, Liu W, Wei C, Chen B, Qi D, Wang H, Wang K, Chen Y, Chen B, Jiang J (2021) Two-dimensional covalent organic frameworks with cobalt(II)-phthalocyanine sites for efficient electrocatalytic carbon dioxide reduction. J Am Chem Soc 143:7104–7113. https://doi.org/10.1021/jacs.1c02145
29 Ji W, Wang T-X, Ding X, Lei S, Han B-H (2021) Porphyrin- and phthalocyanine-based porous organic polymers: from synthesis to application. Coord Chem Rev 439:213875. https://doi.org/10.1016/j.ccr.2021.213875
30 Huang S, Chen K, Li T-T (2022) Porphyrin and phthalocyanine based covalent organic frameworks for electrocatalysis. Coord Chem Rev 464:214563. https://doi.org/10.1016/j.ccr.2022.214563
31. Liang B, Zhao J, Wang J, Li Y, Han B, Li J, Ding X, Xie Z, Wang H, Zhou S (2023) Nonlinear optical properties of porphyrin-based covalent organic frameworks determined by steric-orientation of conjugation. J Mater Chem C 11:3354–3359. https://doi.org/10.1039/D2TC05258J
32. Dong X-Y, Yan F-Q, Wang Q-Y, Feng P-F, Zou R-Y, Wang S, Zang S-Q (2023) A benzimidazole-linked bimetallic phthalocyanine-porphyrin covalent organic framework synergistically promotes CO_2 electroreduction. J Mater Chem A 11:15732–15738. https://doi.org/10.1039/D3TA03023G
33. Li M, Han B, Li S, Zhang Q, Zhang E, Gong L, Qi D, Wang K, Jiang J. Constructing 2D phthalocyanine covalent organic framework with enhanced stability and conductivity via interlayer hydrogen bonding as electrocatalyst for CO_2 reduction. Small. 2024:2310147. https://doi.org/10.1002/smll.202310147
34. Hu H, Miao R, Yang F, Duan F, Zhu H, Hu Y, Du M, Lu S (2024) Intrinsic activity of metalized porphyrin-based covalent organic frameworks for electrocatalytic nitrate reduction. Adv Energy Mater 14:2302608. https://doi.org/10.1002/aenm.202302608
35. Jin E, Asada M, Xu Q, Dalapati S, Addicoat MA, Brady MA, Xu H, Nakamura T, Heine T, Chen Q, Jiang D (1979) Two-dimensional Sp2 carbon-conjugated covalent organic frameworks. Science 2017(357):673–676. https://doi.org/10.1126/science.aan0202
36. Joshi T, Chen C, Li H, Diercks CS, Wang G, Waller PJ, Li H, Bredas J-L, Yaghi OM, Crommie MF (2019) Local electronic structure of molecular heterojunctions in a single-layer 2D covalent organic framework. Adv Mater 31:1805941. https://doi.org/10.1002/adma.201805941
37. Thomas S, Li H, Zhong C, Matsumoto M, Dichtel WR, Bredas JL (2019) Electronic structure of two-dimensional π-conjugated covalent organic frameworks. Chem Mater 31:3051–3065. https://doi.org/10.1021/acs.chemmater.8b04986
38. Thomas S, Li H, Dasari RR, Evans AM, Castano I, Allen TG, Reid OG, Rumbles G, Dichtel WR, Gianneschi NC, Marder SR, Coropceanu V, Brédas J-L (2019) Design and synthesis of two-dimensional covalent organic frameworks with four-arm cores: prediction of remarkable ambipolar charge-transport properties. Mater Horiz 6:1868–1876. https://doi.org/10.1039/C9MH00035F
39. Jiang W, Zhang S, Wang Z, Liu F, Low T (2020) Topological band engineering of lieb lattice in phthalocyanine-based metal-organic frameworks. Nano Lett 20:1959–1966. https://doi.org/10.1021/acs.nanolett.9b05242
40. Pham HQ, Pham-Tran N-N (2021) Topological insulating phase in single-layer pentagonal covalent organic frameworks: a reticular design using metal phthalocyanine. Chem Mater 33:4488–4499. https://doi.org/10.1021/acs.chemmater.1c00671
41. Ni X, Huang H, Brédas J-L (2022) Emergence of a two-dimensional topological dirac semimetal phase in a phthalocyanine-based covalent organic framework. Chem Mater 34:3178–3184. https://doi.org/10.1021/acs.chemmater.1c04317
42. Ni X, Brédas J-L (2022) Electronic structure of zinc-5,10,15,20-tetraethynylporphyrin: evolution from the molecule to a one-dimensional chain, a two-dimensional covalent organic framework, and a nanotube. Chem Mater 34:1334–1341. https://doi.org/10.1021/acs.chemmater.1c04013
43. Lieb EH (1989) Two theorems on the hubbard model. Phys Rev Lett 62:1201–1204. https://doi.org/10.1103/PhysRevLett.62.1201

44. Slot MR, Gardenier TS, Jacobse PH, van Miert GCP, Kempkes SN, Zevenhuizen SJM, Smith CM, Vanmaekelbergh D, Swart I (2017) Experimental realization and characterization of an electronic lieb lattice. Nat Phys 13:672–676. https://doi.org/10.1038/nphys4105
45. Jiang W, Ni X, Liu F (2021) Exotic topological bands and quantum states in metal-organic and covalent-organic frameworks. Acc Chem Res 54:416–426. https://doi.org/10.1021/acs.accounts.0c00652
46. Cui B, Zheng X, Wang J, Liu D, Xie S, Huang B (2020) Realization of lieb lattice in covalent-organic frameworks with tunable topology and magnetism. Nat Commun 11:66. https://doi.org/10.1038/s41467-019-13794-y
47. Jiang W, Huang H, Liu F (2019) A lieb-like lattice in a covalent-organic framework and its stoner ferromagnetism. Nat Commun 10:2207. https://doi.org/10.1038/s41467-019-10094-3
48. Zhang Y, Zhao S, Polozij M, Heine T (2024) Electronic lieb lattice signatures embedded in two-dimensional polymers with square lattice. Chem Sci. https://doi.org/10.1039/D3SC06367D
49. Kollár AJ, Fitzpatrick M, Sarnak P, Houck AA (2020) Line-graph lattices: euclidean and non-euclidean flat bands, and implementations in circuit quantum electrodynamics. Commun Math Phys 376:1909–1956. https://doi.org/10.1007/s00220-019-03645-8
50. Canals B (2002) From the square lattice to the checkerboard lattice: spin-wave and large-n limit analysis. Phys Rev B 65:184408. https://doi.org/10.1103/PhysRevB.65.184408
51. Iskin M (2019) Origin of flat-band superfluidity on the mielke checkerboard lattice. Phys Rev A 99:053608. https://doi.org/10.1103/PhysRevA.99.053608
52. Hu X, Zhang R-W, Ma D-S, Cai Z, Geng D, Sun Z, Zhao Q, Gao J, Cheng P, Chen L, Wu K, Yao Y, Feng B (2023) Realization of a two-dimensional checkerboard lattice in monolayer Cu_2N. Nano Lett 23:5610–5616. https://doi.org/10.1021/acs.nanolett.3c01111
53. Ni X, Li H, Liu F, Brédas J-L (2022) Engineering of flat bands and dirac bands in two-dimensional Covalent Organic Frameworks (COFs): relationships among molecular orbital symmetry, lattice symmetry, and electronic-structure characteristics. Mater Horiz 9:88–98. https://doi.org/10.1039/D1MH00935D
54. Chai J-D, Head-Gordon M (2008) Systematic optimization of long-range corrected hybrid density functionals. J Chem Phys 128:84106. https://doi.org/10.1063/1.2834918
55. Chai J-D, Head-Gordon M (2008) Long-range corrected hybrid density functionals with damped atom-atom dispersion corrections. Phys Chem Chem Phys 10:6615–6620. https://doi.org/10.1039/B810189B
56. Frisch MJ, Trucks GW, Schlegel HB, Scuseria GE, Robb MA, Cheeseman JR, Scalmani G, Barone V, Petersson GA, Nakatsuji H, Li X, Caricato M, Marenich AV, Bloino J, Janesko BG, Gomperts R, Mennucci B, Hratchian HP, Ortiz JV, Izmaylov AF, Sonnenberg JL, Williams-Young D, Ding F, Lipparini F, Egidi F, Goings J, Peng B, Petrone A, Henderson T, Ranasinghe D, Zakrzewski VG, Gao J, Rega N, Zheng G, Liang W, Hada M, Ehara M, Toyota K, Fukuda R, Hasegawa J, Ishida M, Nakajima T, Honda Y, Kitao O, Nakai H, Vreven T, Throssell K, Montgomery Jr JA, Peralta JE, Ogliaro F, Bearpark MJ, Heyd JJ, Brothers EN, Kudin KN, Staroverov VN, Keith TA, Kobayashi R, Normand J, Raghavachari K, Rendell AP, Burant JC, Iyengar SS, Tomasi J, Cossi M, Millam JM, Klene M, Adamo C, Cammi R, Ochterski JW, Martin RL, Morokuma K, Farkas O, Foresman JB, Fox DJ (2016) Gaussian16, Revision C.01. Gaussian Inc. Wallingford CT. https://gaussian.com/citation/
57. Körzdörfer T, Brédas J-L (2014) Organic electronic materials: recent advances in the DFT description of the ground and excited states using tuned range-separated hybrid functionals. Acc Chem Res 47:3284–3291. https://doi.org/10.1021/ar500021t
58. Kresse G, Furthmüller J (1996) Efficiency of Ab-initio total energy calculations for metals and semiconductors using a plane-wave basis set. Comput Mater Sci 6:15–50. https://doi.org/10.1016/0927-0256(96)00008-0
59. Perdew JP, Burke K, Ernzerhof M (1996) Generalized gradient approximation made simple. Phys Rev Lett 77:3865. https://doi.org/10.1103/PhysRevLett.77.3865
60. Perdew JP, Burke K, Ernzerhof M (1997) Generalized gradient approximation made simple. Phys Rev Lett 78:1396. https://doi.org/10.1103/PhysRevLett.78.1396
61 Wang V, Xu N, Liu J-C, Tang G, Geng W-T (2021) VASPKIT: a user-friendly interface facilitating high-throughput computing and analysis using vasp code. Comput Phys Commun 267:108033. https://doi.org/10.1016/j.cpc.2021.108033
62. Momma K, Izumi F (2011) VESTA 3 for three-dimensional visualization of crystal, volumetric and morphology data. J Appl Crystallogr 44:1272–1276. https://doi.org/10.1107/S0021889811038970
63. Ni X, Huang H, Brédas J-L (2022) Organic higher-order topological insulators: heterotriangulene-based covalent organic frameworks. J Am Chem Soc 144:22778–22786. https://doi.org/10.1021/jacs.2c11229
64. Ni X, Li H, Brédas J-L (2024) Half-metallic ferromagnetism in radical-bridged metal-organic frameworks. Chem Mater 36:2380–2389. https://doi.org/10.1021/acs.chemmater.3c03039
65. Liu C-H, Wei A, Cheung MF, Perepichka DF (2022) Vanishing electronic band gap in two-dimensional hydrogen-bonded organic frameworks. Chem Mater 34:3461–3467. https://doi.org/10.1021/acs.chemmater.2c00294
66. Ni X, Yan J, Liu F (2020) Electronic structures of a diagonally striped lattice: multiple (N-1)-fold degenerate flat bands. Phys Rev B 102:235117. https://doi.org/10.1103/PhysRevB.102.235117
67. Wang ZF, Jin K-H, Liu F (2016) Quantum spin hall phase in 2D trigonal lattice. Nat Commun 7:12746. https://doi.org/10.1038/ncomms12746
68. Kane CL, Mele EJ (2005) Quantum spin hall effect in graphene. Phys Rev Lett 95:226801. https://doi.org/10.1103/PhysRevLett.95.226801
69. Kane CL, Mele EJ (2005) Z2 Topological order and the quantum spin hall effect. Phys Rev Lett 95:146802. https://doi.org/10.1103/PhysRevLett.95.146802
70. Fu L, Kane CL (2007) Topological insulators with inversion symmetry. Phys Rev B Condens Matter Mater Phys 76:045302. https://doi.org/10.1103/PhysRevB.76.045302
71. Thouless DJ, Kohmoto M, Nightingale MP, den Nijs M (1982) Quantized hall conductance in a two-dimensional periodic potential. Phys Rev Lett 49:405–408. https://doi.org/10.1103/PhysRevLett.49.405
72. Zhang S, Zhou J, Wang Q, Chen X, Kawazoe Y, Jena P (2015) Penta-graphene: a new carbon allotrope. Proc Natl Acad Sci 112:2372–2377. https://doi.org/10.1073/pnas.1416591112
73. Li F, Tu K, Zhang H, Chen Z (2015) Flexible structural and electronic properties of a pentagonal B2C monolayer via external strain: a computational investigation. Phys Chem Chem Phys 17(37):24151–24156. https://doi.org/10.1039/C5CP03885E
74. Zheng Y, Chen D, Liu L, Liu Y, Chen M, Zhuang H, Jiao Y (2021) Topological transformations in hyperuniform pentagonal two-dimensional materials induced by stone-wales defects. Phys Rev B 103:245413. https://doi.org/10.1103/PhysRevB.103.245413
75. Bravo S, Pacheco M, Nuñez V, Correa JD, Chico L (2021) Two-dimensional weyl points and nodal lines in pentagonal materials and their optical response. Nanoscale 13:6117–6128. https://doi.org/10.1039/D1NR00064K
76. Bravo S, Pacheco M, Correa JD, Chico L (2022) Topological bands in the PdSe2 pentagonal monolayer. Phys Chem Chem Phys 24:15749–15755. https://doi.org/10.1039/D2CP01822E

77. Guo Y, Zhou J, Xie H, Chen Y, Wang Q (2022) Screening transition metal-based polar pentagonal monolayers with large piezoelectricity and shift current. NPJ Comput Mater 8:40. https://doi.org/10.1038/s41524-022-00728-4
78 Shen Y, Wang Q (2022) Pentagon-based 2D materials: classification, Properties and Applications. Phys Rep 964:1–42. https://doi.org/10.1016/j.physrep.2022.03.003
79. Wang M, Ballabio M, Wang M, Lin HH, Biswal BP, Han X, Paasch S, Brunner E, Liu P, Chen M, Bonn M, Heine T, Zhou S, Cánovas E, Dong R, Feng X (2019) Unveiling electronic properties in metal-phthalocyanine-based pyrazine-linked conjugated two-dimensional covalent organic frameworks. J Am Chem Soc 141:16810–16816. https://doi.org/10.1021/jacs.9b07644
80. Zhou J, Wang Q, Sun Q, Kawazoe Y, Jena P (2012) Strain-induced spin crossover in phthalocyanine-based. J Phys Chem Lett 3:3109–3114. https://doi.org/10.1021/jz301303t
81. Li J, Gu L, Wu R (2020) Transition-metal phthalocyanine monolayers as new chern insulators. Nanoscale 12:3888–3893. https://doi.org/10.1039/C9NR09817H
82. Hu T, Zhang T, Mu H, Wang Z (2022) Intrinsic second-order topological insulator in two-dimensional covalent organic frameworks. J Phys Chem Lett 13:10905–10911. https://doi.org/10.1021/acs.jpclett.2c02683

Xiaojuan Ni Xiaojuan Ni currently is a Postdoctoral Research Associate in Chemistry and Biochemistry at The University of Arizona, working with Professor Jean-Luc Bredas. She graduated with Bachelor's (2010) and Master's (2013) degrees in Chemical Engineering and Materials Science from Dalian University of Technology, China. She received her Ph.D. in Materials Science and Engineering from the University and Utah (2020) with the mentorship of Professor Feng Liu. Her research focuses on investigating the geometric, electronic, magnetic, and topological properties of organic frameworks and π-conjugated polymers. Additionally, she explores the ground- and excited-state characteristics of hybrid organic-inorganic perovskites, with a specific emphasis on their potential applications in optoelectronics.

Jean-Luc Bredas Jean-Luc Bredas received his B.Sc. (1976) and Ph.D. (1979) degrees from the University of Namur, Belgium. In 1988, he was appointed Professor at the University of Mons, Belgium, where he established the Laboratory for Chemistry of Novel Materials. While keeping an "Extraordinary Professorship" appointment in Mons, he joined the University of Arizona in 1999. In 2003, he moved to the Georgia Institute of Technology where he became Regents' Professor of Chemistry and Biochemistry and held the Vasser-Woolley and Georgia Research Alliance Chair in Molecular Design. Between 2014 and 2016, he joined King Abdullah University of Science and Technology (KAUST) as a Distinguished Professor and served as Director of the KAUST Solar & Photovoltaics Engineering Research Center. He returned to Georgia Tech in 2017 before moving back to the University of Arizona in 2020 where he is currently Regents Professor in the Department of Chemistry and Biochemistry.

Jean-Luc Bredas is an elected Member of the International Academy of Quantum Molecular Science, the Royal Academy of Belgium, and the European Academy of Sciences. Recent honors include the 2013 American Physical Society David Adler Lectureship Award in the Field of Materials Physics, the 2016 American Chemical Society Award in the Chemistry of Materials, the 2019 Alexander von Humboldt Research Award, the 2020 Materials Research Society Materials Theory Award, and the 2021 Centenary Prize of the Royal Society of Chemistry. He is an Honorary Professor of the Institute of Chemistry of the Chinese Academy of Sciences and holds an Adjunct Professorship at the Georgia Institute of Technology. He was Editor for *Chemistry of Materials*, published by the American Chemical Society, between 2008 and 2021; since June 2022, he serves as Scientific Editor for *Materials Horizons*, the flagship materials journal of the Royal Society of Chemistry. He has published over 1200 scientific articles, which have garnered nearly 140000 citations (h-index: 170) according to Google Scholar.